Dynamic Measurement of Gas Flow using Acoustic Resonance Tracking

Jodie G. Pope[a,b], James W. Schmidt[a], and Keith A. Gillis[a]

[a]Sensor Science Division, Physical Measurement Laboratory, National Institute of Standards & Technology, 100 Bureau Dr., Gaithersburg, MD 20899

[b]Corresponding author: jodie.pope@nist.gov

Abstract

The National Institute of Standards and Technology (NIST) measured gas flows exiting large, un-thermostated, gas-filled, pressure vessels by tracking the time-dependent pressure $P(t)$ and resonance frequency $f_N(t)$ of an acoustic mode N of the gas remaining in each vessel. This is a proof-of-principle demonstration of a gas-flow standard that uses $P(t)$, $f_N(t)$, and known values of the gas's speed-of-sound $w(p,T)$ to determine a mode-weighted average temperature $\langle T\rangle_\varphi$ of the gas remaining in a pressure vessel while the vessel acts as a calibrated source of gas flow. To track $f_N(t)$ while flow work rapidly changed the gas's temperature, we sustained the gas's oscillations using positive feedback. Feedback oscillations tracked $\langle T\rangle_\varphi$ with a response time of order $1/f_N$. In contrast, driving the gas's oscillations with an external frequency generator yielded much slower response times of order Q/f_N. (For our pressure vessels, $Q \sim 10^3$ to 10^4, where Q is the ratio of the energy stored to the energy lost in one cycle of oscillation.) We tracked $f_N(t)$ of radial modes in a spherical vessel (1.85 m^3) and of longitudinal modes of a cylindrical vessel (0.3 m^3) during gas flows ranging from 0.24 g/s to 12.4 g/s to determine the mass flows with an uncertainty of 0.51 % (95 % confidence level). We discuss the challenges in tracking $f_N(t)$ and ways to reduce the uncertainties.

The data that support the findings of this work are available from the corresponding author upon reasonable request.

I. Introduction and Background

Primary gas flow standards measure the change of the mass of a gas in a measured volume (V) during a designated time interval, sometimes with uncertainties < 0.1 % [1]. Gravimetric gas flow standards weigh a pressure vessel to determine the change in mass while volumetric standards calculate the mass by multiplying the gas's average density by the internal volume of the vessel. The gas density is calculated from an equation of state for the gas species, the measured gas pressure, and the spatial average temperature of the gas in the vessel $\langle T\rangle_V$. The average temperature is challenging to measure accurately: flow work causes the temperature of the gas in the vessel to increase (or decrease) when gas is added to (or discharged from) the measuring vessel causing spatial temperature gradients that change over time.

Several approaches have been applied to obtain $\langle T\rangle_V$ with acceptably small uncertainty. The National Institute of Standards and Technology (NIST) has gas flow standards that measure $\langle T\rangle_V$ by three methods.

NIST's 26 m^3 pressure, volume, temperature, and time (*PVTt*) standard averages 37 strategically located temperature sensors to obtain $\langle T \rangle_V$, but the average temperature measurement is the largest source of the mass flow uncertainty (0.09 %[1]) [2,3]. NIST's 0.034 m^3 and 0.677 m^3 flow standards (0.025 % mass flow uncertainty) obtain smaller average temperature uncertainty by containing the gas within a measuring vessel that has a high surface-to-volume ratio and immersing the vessel in a temperature-controlled water bath [4]. This standard is useful for relatively low flows (< 2000 L/min) and pressures up to 700 kPa at the standard's entrance.

Here, we advance a third method for obtaining $\langle T \rangle_V$; we measure acoustic resonance frequencies and the pressure to determine the average gas temperature in a measuring vessel of known dimensions [5,6,7,8,9]. The mass of gas measured acoustically M_{acst} is determined from the gas pressure, an acoustic resonance frequency f_N of the gas and the dimensions of the measuring vessel combined with the gas's thermodynamic properties [Eq. (3)]. For larger gas flows (>2000 L/min), the size, weight, and pressure rating of a measuring vessel increase significantly; submerging the vessel in a water bath is impractical. The acoustic method has the potential to determine the average temperature with low uncertainty without a thermostated water bath.

In reference [5], we used NIST's 0.025 % uncertainty *PVTt* standards to calibrate critical flow venturis (CFVs) and used them as references to validate our new acoustic flow measurement techniques. In that work, we made static gas flow measurements, *i.e.*, we measured the mass acoustically before flow from the measuring vessel started and long after flow stopped; therefore, the temperature distribution in the vessel was nearly steady. The static acoustic flow measurements and the CFVs agreed within 0.053 % for flows up to 59 g/s. However, the time it took to obtain nearly steady temperature conditions was too long to be practical as a gas flow standard.

Dynamic flow methods measure the rate of change of the mass of gas in the vessel while the tank is filling or discharging [1] using a simple on / off valve instead of a complex flow diverter used in a *PVTt* standard [1,10]. A challenge for dynamic gas flow standards for large flows is that the temperature conditions in the vessel are changing spatially and temporally, making it difficult to measure $\langle T \rangle_V$ [11].

Here, we demonstrate a method to track an acoustic resonance frequency $f_N(t)$ during gas flow out of a pressure vessel that allows us to determine the mass flow $\dot{m}_{\mathrm{acst}} = dM_{\mathrm{acst}}/dt$. We used the vessel as a gas

[1] All uncertainties are stated as approximately 95 % confidence level values unless otherwise stated. We use the terminology "expanded" uncertainty for approximately 95 % confidence level values, and "standard" uncertainty for approximately 68 % confidence level values.

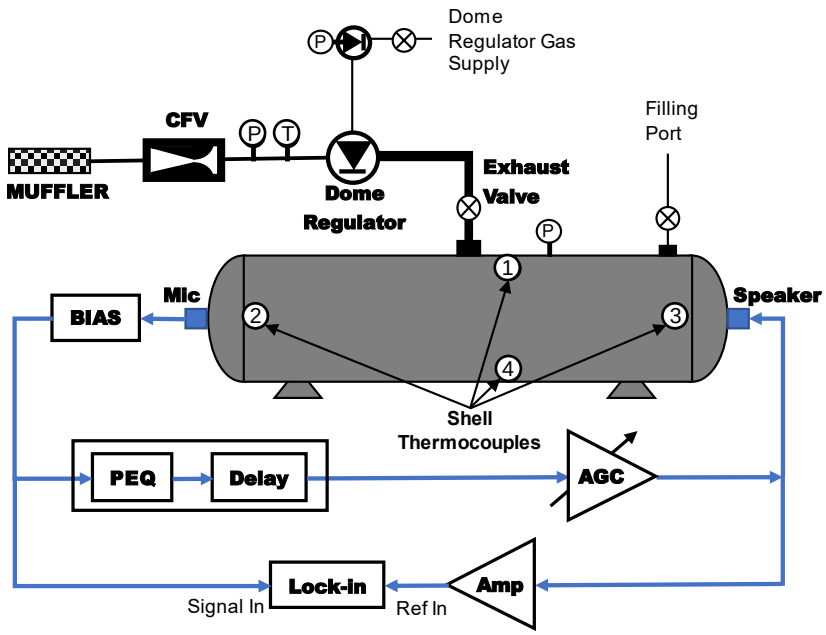

Fig. 1. Schematic circuit to achieve self-oscillation of acoustic waves in a pressure vessel using positive feedback. The circuit includes a microphone (Mic), a speaker, an amplifier (Amp), an automatic gain control (AGC), a bandpass filter (parametric equalizer, PEQ), a phase adjustment (Delay), and a lock-in amplifier (Lock-in). We used the same circuit for both vessels used in this work. During operation, gas flows from the vessel through the dome pressure regulator and through a critical flow venturi (CFV) acting as a meter under test (MUT).

source, not a collection volume. When used as a collection volume, the noise generated by the incoming gas made it too difficult to isolate an acoustic frequency of interest. Furthermore, the incoming expanding gas forms a jet with large temperature gradients and complicated flow patterns. Unlike other resonance mode tracking applications [12,13,14,15,16,17], we used an acoustic resonator as the frequency-determining component in the self-oscillating feedback circuit, as shown in Fig. 1 [18].

Self-oscillating resonators are not new [19], however, to the authors' knowledge, self-oscillations have never been applied to a pressure vessel while gas flows into or out of it. We showed the successful tracking during gas flow by self-oscillation of 1) longitudinal resonance modes in a cylindrical geometry and 2) radial resonance modes in a spherical geometry. In contrast to previous work at NIST [20,21] with resonators having machined and polished internal surfaces, the cylindrical and spherical vessels we used have large surface and shape imperfections. We found the cylindrical geometry is better for tracking in a dynamic gas flow standard for reasons we will discuss below. The dynamic $\dot{m}_{\mathrm{acst}}$ from the cylindrical geometry differed from calibrated CFVs $\dot{m}_{\mathrm{CFV}}$ within 0.73 %, which is within the combined, expanded uncertainty for the acoustic gas flow and the measured flow through a CFV. The uncertainty ranges from 0.54 % to 0.93 % depending on flow. Figure 2 shows these results graphically. One possible explanation

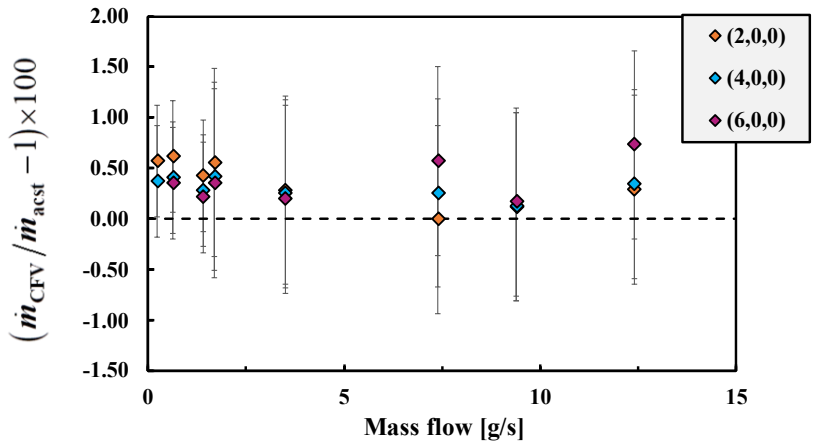

Fig. 2. The percent difference between mass flow measured from calibrated CFVs $\dot{m}_{CFV}$ and dynamic acoustic mass flow $\dot{m}_{acst}$ for the three longitudinal modes (2,0,0), (4,0,0), and (6,0,0). The largest contribution to the acoustically determined mass flow uncertainty is the standard deviation in the repeated measurements of each mode. It contributes approximately 79 % to the overall uncertainty and is 0.23 % as shown in Table 1. The uncertainty budget is discussed in Section IV. The standard deviation is on the same order as the average offset in $\dot{m}_{acst} - \dot{m}_{CFV}$, therefore, we combine these into one uncertainty component. The data points represent a minimum of three repeated measurements. The standard deviation of all measurements of each mode at each flow was taken and the maximum value over the flows tested was used in our uncertainty budget.

for the offset and variance in the agreement between $\dot{m}_{CFV}$ and $\dot{m}_{acst}$ is due to complicated and irreproducible temperature gradients in the vessel during flow.

Our target uncertainty for $\dot{m}_{acst}$ is 0.08 %. Based on our preliminary results and past work [22] we believe that we can achieve this uncertainty with optimized tank geometry and construction, *i.e.*, weld locations, wall thickness, and gas entry/exit locations. The uncertainty is discussed in Section IV.

In this manuscript we discuss resonance techniques and review our reasons for using self-oscillations to track $f_N(t)$ to measure $\langle T \rangle_V$ dynamically during gas flows. We discuss Fig. 2 and the uncertainty in our measurements. In Section III, we argue that the approximately +0.4 % offset and deviation between $\dot{m}_{acst}$ and $\dot{m}_{CFV}$ may be due to axial temperature gradients that might be improved with a judicious location of the gas exhaust tube.

Resonance techniques

Resonance techniques are advantageous because frequencies can be measured with high precision. In previous publications [5,6,7,8,9], we showed that the mass of gas in a closed metal vessel with cylindrical or spherical geometry can be determined from the vessel's dimensions combined with measurements of the pressure and the internal gas's speed of sound using resonance techniques [21,23]. The measurements were made when the vessel and the enclosed gas were in thermal equilibrium with the room. This is of the upmost

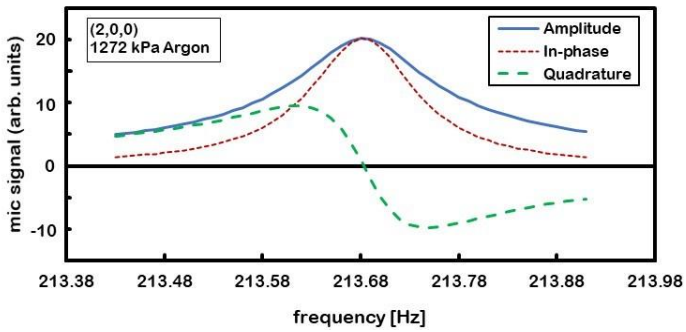

Fig. 3. Scan of the (2,0,0) longitudinal acoustic mode in cylindrical tank filled with argon at 1.3 MPa. A fit to the data gave f_N = 213.6840 Hz ± 0.0004 Hz and g = 0.0665 Hz ± 0.0004 Hz. The quality factor for this mode was Q = 1600. It took about 12 min to do the scan of 49 data points in one direction at 14 sec/point. The shell temperature changed by less than 24 mK during this scan.

importance because the frequency changes with temperature. Conventionally, measurements of the in-phase and quadrature signal voltages are acquired using a lock-in amplifier at a set of discrete frequencies in the vicinity of an acoustic mode (identified by a set of numbers N). The data are then fitted with a resonance response function (discussed elsewhere [8,20,21,23]) by adjusting an amplitude, the resonance frequency f_N, the resonance halfwidth g, and background terms. After gas flow into or out of the vessel, there is a significant temperature drift, and a quasi-steady state may take hours to reach (see Section II). In this case, response measurements at discrete frequencies are an impractical method to determine a resonance frequency.

Figure 3 shows a plot of the frequency response of a longitudinal mode in the cylindrical tank. The in-phase and quadrature components and the amplitude are plotted as a function of frequency. In thermal equilibrium, the minimum dwell time for accurate measurement is determined by the longest relaxation time, which is either the resonance's characteristic transient response time $\tau_r = 1/(2\pi g) \approx 2.4$ s for g = 0.066 Hz or the lock-in amplifier's post-detection time constant (30 ms for this work). For resonances with small g (high quality factor Q [24]), sufficient time ($\sim 6\tau_r$) must elapse to achieve a quasi-steady state before the signal is measured (14 sec per point for the mode in Fig. 3). A fit to the data in Fig. 3 gave an uncertainty of ± 0.0004 Hz in f_N and g. The shell temperature changed by no more than 24 mK during this scan, which corresponds to 0.009 Hz change in frequency and hence the high-resolution scan is possible.

Pressure vessels as acoustic resonators

As mentioned previously, we made acoustic temperature measurements in two pressure vessels with different geometries (cylindrical and spherical). The cylindrical vessel is a 0.3 m³ commercially manufactured tank with ellipsoidal heads with a maximum working pressure of 1.4 MPa. It has a smooth

inner surface with exceptions at the welds near the ports, the endcaps, and a seam along its length. The spherical vessel, called the Big Blue Ball (BBB), has a volume of 1.8 m³ and a maximum working pressure of 7 MPa [5,6]. The BBB has significant rust and pitting on its interior surface, welded ports, and a circumferential weld around its equator. Poor surface conditions, ports, and welds make these vessels non-ideal resonators. [20,22]. Despite the above imperfections, we measured the acoustic and microwave resonance frequencies to obtain the speed of sound and volume, respectively, using acoustic and electromagnetic resonance models of both vessels [5,6,7,8,9].

The low-frequency speed of sound w in a gas is a thermodynamic property that is a function of the gas temperature and pressure; it is conveniently written as a pressure expansion for the dilute gas

$$w^2(T,P) = \frac{\gamma_0 RT}{M_w}\left[1 + \frac{\beta_a P}{RT} + \ldots\right] = \frac{\gamma_0 RT}{M_w}\mathcal{Z}_{\text{acst}}(T,P) \tag{1}$$

where $\gamma_0 \equiv C_P/C_V$ is the zero-pressure heat-capacity ratio, R is the universal gas constant, M_w is the molar mass, T is the gas temperature, P is the gas pressure, and β_a is the second acoustic virial coefficient. The quantity $\mathcal{Z}_{\text{acst}}(P,T) = M_w w^2/(\gamma_0 RT)$ is analogous to the compression factor $Z(P,T) = M_w P/(\rho RT)$ for the equation of state. We determine $w(T, P)$ acoustically from the resonance frequency $f_N(T,P)$ of the gas using the relation

$$w(T,P) = 2\pi f_N(T,P)/k_N\ , \tag{2}$$

where k_N is the known wavenumber for the mode N. k_N is determined from acoustic theory for the vessel shape or from calibration with a reference gas, such as argon [9]. We combined the virial expansion of the equation of state for gas density $\rho(T,P)$, the pressure expansion for $w^2(T,P)$ from Eq. (1), and Eq. (2) to obtain an expression for the mass M_{acst} of gas in a closed vessel

$$M_{\text{acst}} = \frac{\gamma_0 k_N^2 V_{\text{tank}}}{4\pi^2}\frac{P}{f_N^2}\left[1 + (\beta_a - B)\frac{P}{RT} + \ldots\right] = \frac{\gamma_0 k_N^2 V_{\text{tank}}}{4\pi^2}\frac{P}{f_N^2}\frac{\mathcal{Z}_{\text{acst}}}{Z}\ . \tag{3}$$

The mass flow $\dot{m}_{\text{acst}}$ (= dM_{acst}/dt) is, therefore, proportional to the time derivative of P/f_N^2.

In [9], we showed that the mass of gas in vessels can be determined from Eq. (3) even with a large, steady temperature gradient present. In [7], we determined the leak rate of argon gas out of the unthermostated cylindrical tank with a relative uncertainty of 0.32 % by monitoring the acoustic resonance frequency and the pressure as a function of time while the tank, located outdoors, experienced sunshine-driven temperature gradients for 3 days. We argue that convection currents within a thin boundary layer near the tank wall left a stable, vertical, linear temperature gradient within the core of the tank. In the BBB, the mass of 99.999 % pure argon was measured acoustically over the pressure range of 0.66 MPa to 6.96 MPa with an expanded

uncertainty of 0.050 % [5]. These measurements were under static or quasi-equilibrium conditions where we let the gas reach thermal equilibrium with the environment and hence the gas temperature had an approximately linear gradient from top to bottom. We initially started using the BBB as a static gas flow standard and found a long waiting period (> 5 h) was required to achieve a spatially linear temperature gradient and an acoustically measured mass within 0.01 % of its equilibrium value.

II. Frequency Tracking Techniques

In this section, we describe three methods to measure the acoustic resonance frequency that are faster than a frequency scanning approach and we discuss their suitability for dynamic gas flow standards.

Tracking using a PID loop

We can determine f_N more quickly if, instead fitting the mode's frequency response, we use the quadrature component of the lock-in output as an error signal for a proportional-integral-differential (PID) loop. This method requires an initial adjustment of the lock-in phase to zero the quadrature when $f = f_N$. Then, when the speed of sound in the gas changes, the magnitude and sign of the error signal are used to adjust the drive frequency to bring the quadrature component back to zero.

The ability of the algorithm to track $f_N(t)$ is determined by the update interval of the PID loop (~1 s) and the transient response time of the resonance τ_r ($\approx$ 16 s for g = 0.01 Hz). As $f_N(t)$ changes with the drive frequency fixed, the oscillations take ~ $6\tau_r$ (100 s for this example) to adjust to the new response amplitude. If $f_N(t)$ changes too quickly, then the amplitude will not have sufficient time to readjust, and the tracking algorithm will lag the true resonance frequency. Therefore, this method is not acceptable for a dynamic gas flow standard because the temperature changes too quickly.

Natural Frequency and Ringdown

Undriven oscillations in a resonator can only be a superposition of the resonator's natural frequencies [32]. Therefore, when a standing wave is established and the sound source is disconnected, the subsequent decaying oscillations (ringdown) must be at the natural frequency. Ringdown measurements of eigen-frequencies are not new [25,26,27,28], however, this is the first time to our knowledge that it has been applied to a flow standard. Ringdown of resonators provides a method to ensure that the phase ϕ of the sound source is set properly, *i.e.*, that the source is synchronous with the waves in the resonator. The signal to the sound source can come from either a function generator or a feedback loop.

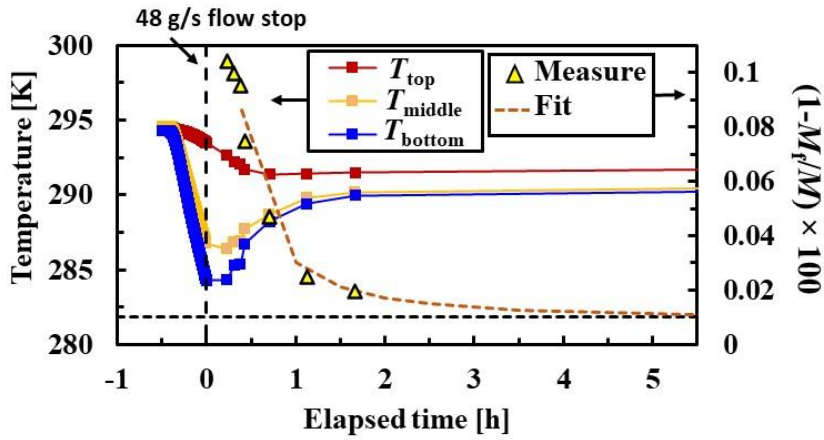

Fig. 4. Temperature gradients in the BBB measured from uncalibrated surface thermistors. The vertical dashed line shows when the 48 g/s flow stopped. The squares on the temperature traces correspond to the yellow triangles, which are when ringdowns where performed. The horizontal dashed line corresponds to the right axis and shows where 0.01 % is. The pressure changed from 5.8 MPa to 2.2 MPa during the flow that lasted for 0.5 h.

We previously determined that ringdown measurements of acoustic resonance frequencies gave a much faster method to measure $\langle T \rangle_V$ in vessels and are as accurate as traditional acoustic frequency scans [5]. We used ringdown measurements to determine M_{acst} under static conditions before and after a flow, however, this method is still too slow as we discuss here.

We showed in [6] that flow work from gas entering or leaving the BBB generates unstable, difficult-to-measure temperature gradients that can last for several days. Figure 4 shows the surface temperature of the BBB during and following a 48 g/s nitrogen flow that lasted for 0.5 h out of the BBB. Ringdowns were performed at the times post flow indicated by the yellow triangles. The dashed line is a fit of a decaying exponential function to the ringdowns. A final mass was determined approximately two days after the flow stopped, well after a stable temperature stratification of the gas was established. According to our fit, the final mass could be determined within < 0.01 % after waiting 5.5 h after the flow stopped when using the ringdown method. This amount of time is not practical, and a dynamic flow standard is preferred.

Sustained Self-Oscillation

An alternative method to a PID loop is to track the resonance frequency using a self-oscillating feedback circuit with the acoustic resonator as the resonant element, as shown in Fig. 1 [18]. This is the method we used for the dynamic flow standard.

In this method, the microphone signal is filtered, amplified, and fed back to the speaker synchronously with the acoustic field in the resonator, thereby creating positive feedback. If the overall gain of the feedback

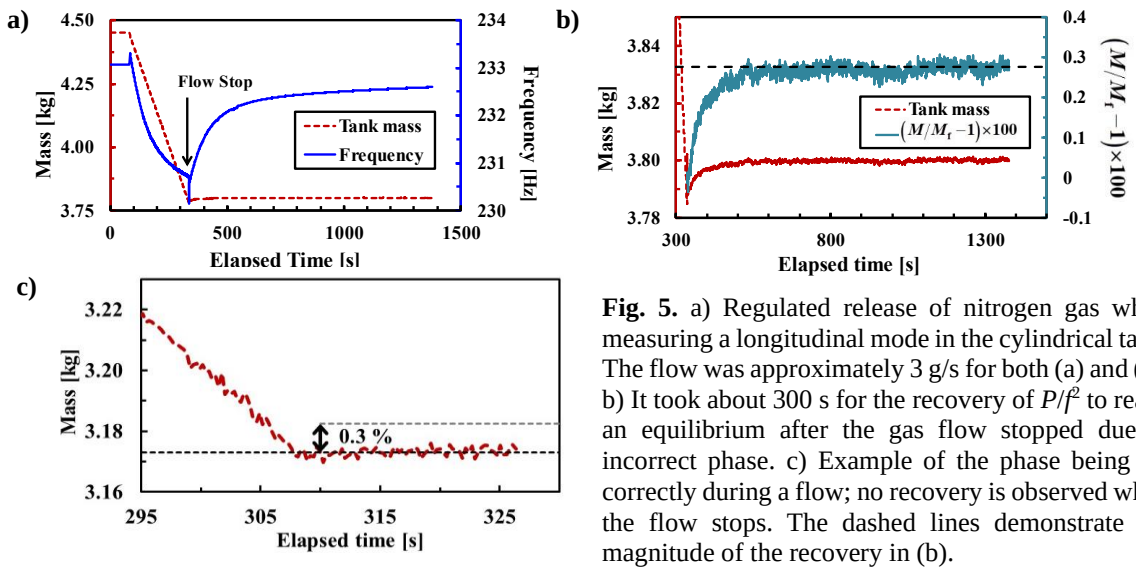

Fig. 5. a) Regulated release of nitrogen gas while measuring a longitudinal mode in the cylindrical tank. The flow was approximately 3 g/s for both (a) and (b). b) It took about 300 s for the recovery of P/f^2 to reach an equilibrium after the gas flow stopped due to incorrect phase. c) Example of the phase being set correctly during a flow; no recovery is observed when the flow stops. The dashed lines demonstrate the magnitude of the recovery in (b).

circuit is greater than one, then the oscillations are self-sustaining at f_N. Since the frequency of the oscillations in the resonator is determined by the average speed of sound, the oscillations are locked to the instantaneous natural frequency as the speed of sound changes. The frequency changes synchronously within an oscillation period $1/f_N \approx 4$ ms [29], thereby avoiding transients with long decay times [22].

Because positive feedback with gain greater than unity creates exponentially growing amplitude, one or more of the elements in the feedback circuit will eventually reach the limit of its linear range, causing distortion or failure. To avoid this problem, we compress the dynamic range of the signal using an automatic gain control (AGC), shown in Fig. 1, that adjusts the gain of the loop to maintain a stable oscillation amplitude [30]. The circuit for the AGC is discussed in Appendix A (the response time ~0.02 s). The PEQ filter shown in Fig. 1 is needed to select the desired mode by suppressing frequencies outside of a chosen bandwidth. Without the filter, the feedback circuit would oscillate at the frequency of the mode with the largest amplitude (determined by the transducer locations and by the frequency response of the transducers and the amplifier). To ensure that the feedback signal is synchronous with the acoustic fields, we adjust the phase ϕ to compensate for phase shifts introduced by the transducers, the filter, or the amplifier, thereby maximizing the amplitude of the signal. The frequency changes during flow and the delay Δt is adjusted to keep the phase of the feedback signal constant ($\phi = 2\pi f \Delta t$).

We learned from our measurements in the cylindrical tank that the phase of the feedback needs to be adjusted as the frequency changes to avoid a "recovery" phenomena that can lead to an error in our flow measurement because the slope of the mass versus time will be wrong. This phenomenon was not observed in the BBB, presumably because both the source and detector were on the periphery of the sphere. Thus,

they interacted with the pressure wave at the same phase. Figure 5a shows the mass in the tank ($\propto P/f_N^2$) and the tracked $f_N(t)$ without correcting the phase during a flow of approximately 3 g/s. Figure 5b shows the difference in the final mass at the time the flow stopped, M_f, from the instantaneously measured mass. It took approximately 300 s for the measured mass to reach an equilibrium, which is 0.3 % different from M_f. We also computed the mass flow from f_N before and after flow from the tank (under equilibrium conditions) and dividing by the flow time, similar to the *PVTt* method described above. We compared this to the flow calculated from dM_{acst}/dt as shown in Fig. 5a. The difference is 0.83 %. (2.60 g/s from dM_{acst}/dt, 2.58 g/s from *PVTt* method.)

For the measurements described here, we used a digital parametric equalizer (Behringer DEQ2496[2]) to create a configurable set of filters and delay to allow only the desired acoustic resonance to be self-sustaining. Additional amplification of the processed signal with an audio amplifier (JBL CSA 1120Z) was necessary when using the BBB as a resonator. The circuit with positive feedback will, therefore, track $f_N(t)$ in the resonator as the speed of sound changes due to changes in the temperature. The lock-in amplifier (Stanford Research Systems SR850) in Fig. 1 is used to measure the instantaneous f_N, the amplitude, and the phase of the oscillations in the feedback circuit.

III. Dynamic Flow Measurements Using Self-Oscillation

Acoustic self-oscillations in the BBB

We used a similar apparatus as shown in Fig. 1 to track $f_N(t)$ of radial modes in the BBB during unregulated flow of nitrogen gas [31]. We were able to successfully track flows when the rate was less than 1 g/s, however, when the flow was increased by an order of magnitude, tracking failed. The reasons why tracking failed are 1) the temperature in the BBB was changing more rapidly than at flows of 1 g/s, which requires faster manual manipulation of the filtering equipment, 2) the temperature distribution in the BBB becomes more unstable as flow time progresses; this is more severe for larger flows, and 3) the radial mode drops in amplitude due to flow noise [32], which channels acoustic energy into multiple other modes. The difficulty imposed by this drop in amplitude is compounded by the fact that nearby modes that have at least an order of magnitude larger amplitude than the radial modes become easier to couple to because our filter cannot filter them out.

[2] In order to describe materials and procedures adequately, it is occasionally necessary to identify commercial products by manufacturers' name or label. In no instance does such identification imply endorsement by the National Institute of Standards and Technology, nor does it imply that the particular product or equipment is necessarily the best available for the purpose.

We decided a cylindrical geometry would be better for acoustic resonance tracking because the longitudinal modes are 1) greatly separated from neighboring modes and 2) the acoustic averaging of longitudinal modes in the presence of vertical temperature gradients is closer to the volume averaged temperature than in a spherical geometry [6]. Furthermore, we believe that the tracking measurement may be immune to complicated temperature gradients or to the plume of cold gas that leaves the tank if the exhaust port location is carefully chosen, as discussed below.

Acoustic self-oscillations in the cylindrical tank

Figure 1 shows the experimental apparatus that we used with the cylindrical tank to compare the acoustic flow measurements, Eq. (3), with the flow obtained from CFVs calibrated with NIST's flow standards. Figure 6a shows the measured $P(t)$ and $f_N(t)$ in the cylindrical tank for a preliminary measurement. The plot is divided into five time periods: quiescent, fill, leak, flow, and recovery. After the quiescent period, the tank was pressurized (as indicated by the blue curve in Fig. 6a) with nitrogen. The green curve in Fig. 6a is

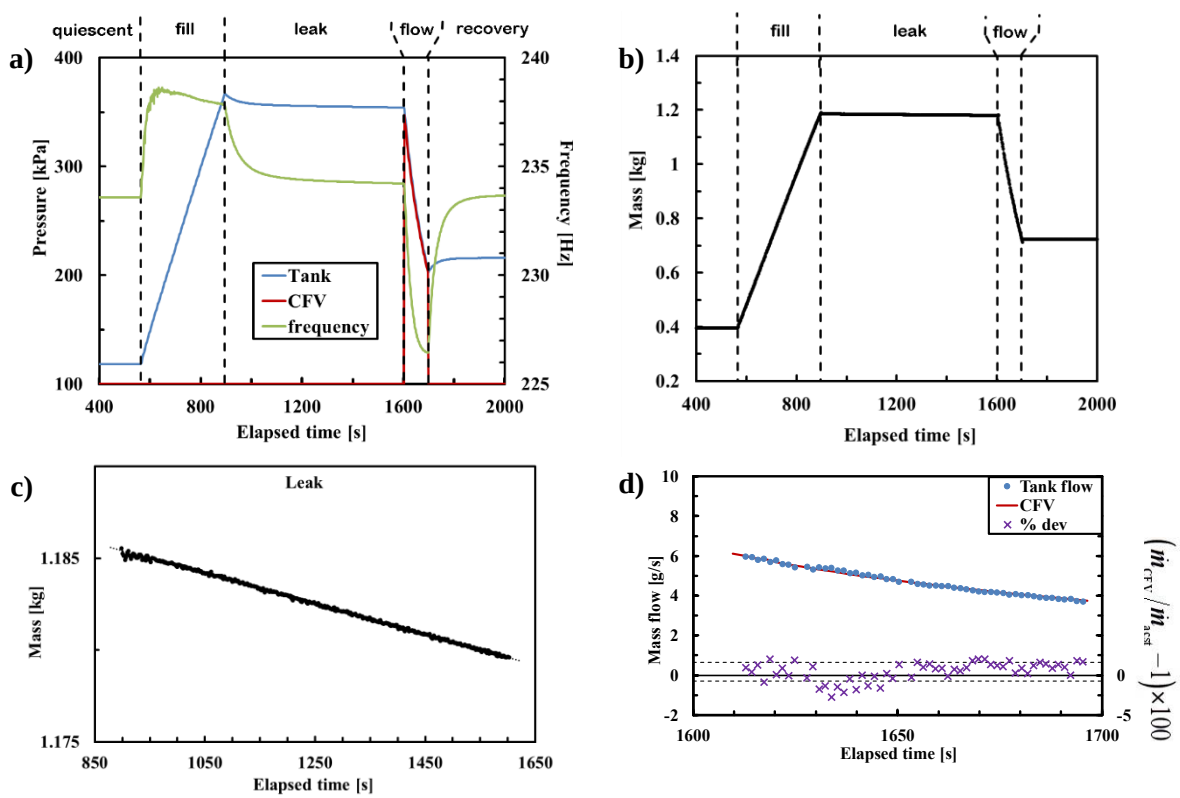

Fig. 6. Validation with a CFV in the cylindrical tank. a) Pressure in the tank (blue), CFV (red), and the resonance frequency in the tank (green) as a function of time. Shows filling, a leak after filling, outward flow, and recovery. b) Same data as in a) showing calculated mass in tank versus time based on acoustic measurements. c) Close up of mass versus time in the leak region after filling was stopped. Calculated leak rate was 8.3 ± 0.016 mg/s. d) (top) Mass flow versus time in the flow region calculated from acoustic measurements and from CFV. (bottom) percent deviation between acoustic and CFV flow determinations. The dashed lines are the standard deviation (1.2 %) above and below the average percent deviation (0.43 %).

$f_N(t)$ for the (2,0,0) longitudinal mode. (We only measured even-numbered longitudinal modes because they do not require correction for center-of-mass motion [9].) Figure 6b shows the instantaneous M_{acst} in the tank $\left(\propto P/f_N^2\right)$ from Eq. (3). When the flow stopped after filling the vessel, the pressure was monitored to check for leaks. The pressure drop during this period is due to a combination of a gas leak and the dropping temperature after the end of flow. M_{acst} during the leak segment is shown in detail in Fig. 6c. After the leak period, we began unregulated flow through the CFV. Figure 6d shows $\dot{m}_{\mathrm{acst}}$, $\dot{m}_{\mathrm{CFV}}$, and their agreement starting 10 s after flow began until the flow is stopped.

Following our preliminary test, we used a regulator to control the discharge pressure from the cylindrical tank. The regulator provides a stable mass flow; therefore, a fit of $M_{\mathrm{acst}}(t)$ is a straight line whose slope is $\dot{m}_{\mathrm{acst}}$. Figure 7 shows $M_{\mathrm{acst}}(t)$ and $P(t)$ as nitrogen gas flowed out at a constant rate of 12.4 g/s.

We tested flows ranging from 0.24 g/s to 12.4 g/s using a series of calibrated CFVs to compare with $\dot{m}_{\mathrm{acst}}$ using the (2,0,0), (4,0,0), and (6,0,0) modes. Figure 2 summarizes these results. The expanded uncertainty in $\dot{m}_{\mathrm{acst}}$ is 0.52 %, with the largest contribution being from the variance in the acoustic measurements. We believe this variance is due to complicated and irreproducible axial temperature gradients in the cylindrical tank during flow [6,9]. We discuss our reasoning below.

In Eq. (3), we calculate the mass of gas in a vessel from $\rho(P,T)V$. We measure the pressure directly. We determine the temperature from w that we measure with one or more acoustic resonance frequencies. In a volume of gas with uniform temperature, ρ, T, and w are independent of position. When the temperature is not uniform, then ρ and w are spatially dependent. The density must be averaged over the volume, $\langle\rho\rangle_V \propto \langle 1/T\rangle_V$. Because typical spatial temperature fluctuations $\delta T(\mathbf{r})$ are small compared to the average

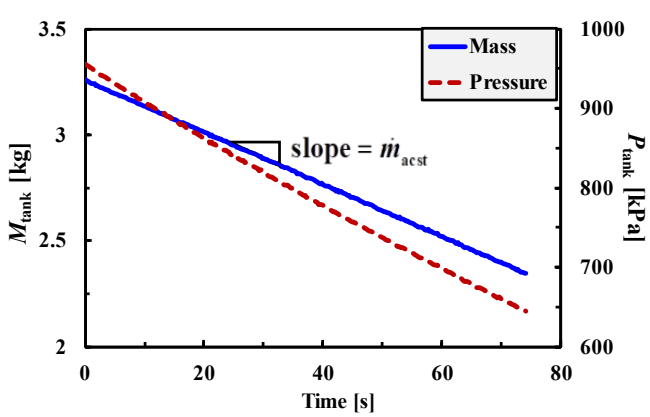

Fig. 7. Example of steady flow via the use of a regulator at the cylindrical tank outlet. The slope of the acoustic mass versus time gives the mass flow rate $\dot{m}_{\mathrm{acst}}$.

temperature, *i.e.* $\delta T(\mathbf{r}) << \langle T\rangle_V$, we can approximate $\langle 1/T\rangle_V \approx 1/\langle T\rangle_V$ with small corrections on the order of$[\sigma_T / \langle T\rangle_V]^2$, where σ_T is the standard deviation of the temperature fluctuations. To first order, the resonance frequencies are determined by a mode-dependent, weighted average of $[w(\boldsymbol{r})]^2$ over the volume. The average temperature $\langle T\rangle_\varphi$ determined from the acoustic measurements is also a weighted average

$$\langle T\rangle_\varphi = \frac{\int_V T(\mathbf{r})|\varphi_N|^2\, dV}{\int_V |\varphi_N|^2\, dV} \quad , \tag{4}$$

where φ_N is the velocity potential (proportional to the acoustic pressure) for mode N and $\mathbf{r}$ is the position vector. In this work we consider only the longitudinal modes (l,0,0) that are symmetric about $z = 0$, *i.e.*, l is an even integer. For simplicity from here on, we use subscript l instead of N to identify the longitudinal mode (l,0,0). $|\varphi_l|^2$ for $l = 2$ is plotted in Fig. 8.

In previous publications [6,9], we explored the difference between $\langle T\rangle_\varphi$ and the evenly weighted volume average temperature $\langle T\rangle_V$ that we need for $\langle\rho\rangle_V$. We showed that the geometry of the vessel, the symmetry of the measured acoustic modes, and the spatial dependence of the temperature gradients influenced the magnitude of $[\langle T\rangle_\varphi - \langle T\rangle_V] / \langle T\rangle_V$. Specifically, for a horizontal cylindrical vessel with a vertical (linear or nonlinear) temperature gradient, the average temperature measured with longitudinal modes is the same as the volume average temperature. A vertical temperature gradient will likely manifest when the vessel and its enclosed gas are left alone to achieve quasi-equilibrium with the environment. However, when the gas flows into or out of the vessel, much more complicated gradients form. These gradients are unknown and may change from flow to flow.

Spatial temperature modeling

The exhaust port for the cylindrical tank is located on the top side midway between the heads, as shown in Fig. 1. The expansion of the gas as it flows out through the exhaust port causes the gas in the tank to cool. We expect both horizontal and vertical temperature gradients to develop. Because it is difficult to measure the temperature distribution inside the tank, we can only speculate about the temperature distribution based on external sensors and on the average acoustic temperature. Based on this information, we created simplistic models of the temperature distribution in a horizontal tank, assumed to be a right circular cylindrical shell with length $L = 150$ cm, radius $R = 25$ cm, and an exhaust port located at the axial coordinate $z = z_P$. The models divide the tank into regions 1 and 2 with volumes V_1 and V_2 and temperatures T_1 and $T_2 < T_1$, respectively. To estimate the uncertainty in our flow measurements, we used the fractional difference $[\langle T\rangle_\varphi - \langle T\rangle_V] / \langle T\rangle_V$ where

$$\langle T\rangle_V = \frac{1}{V}\left(T_1V_1 + T_2V_2\right) = T_1 - \frac{V_2}{V}\Delta T \ , \tag{5}$$

$$\langle T\rangle_\varphi = \frac{1}{V\Lambda_l}\left[T_1\int_{V_1}|\varphi_l|^2\,dV + T_2\int_{V_2}|\varphi_l|^2\,dV\right] = \langle T\rangle_V + \Delta T\left[\frac{V_2}{V} - \frac{1}{V\Lambda_l}\int_{V_2}|\varphi_l|^2\,dV\right] \ , \tag{6}$$

with $V = \pi R^2 L = V_1 + V_2$ and $\Delta T = T_1 - T_2$. We chose the in longitudinal modes with even integer l, which are symmetric about $z = 0$, whose velocity potential is

$$\varphi_l = \cos\left(l\pi z/L\right) \tag{7}$$

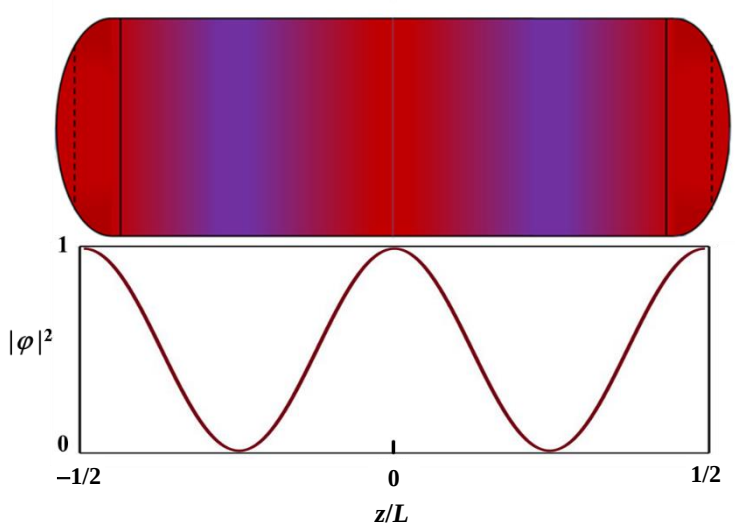

Fig. 8. Square of the velocity potential $|\varphi_l|^2$ (proportional to the acoustic pressure) for (2,0,0) mode in the cylindrical tank. z/L is the fractional distance along the tank's length. The velocity potential is zero at acoustic nodes (purple) and 1 at acoustic antinodes.

with normalization $\Lambda_l = \frac{1}{2}$. The measurements in this work correspond to a centrally located exhaust port ($z_P = 0$). For the design of future vessels, we explored locating the exhaust port off-center ($z_P \neq 0$). More details are given in Appendix B.

<u>The plume model</u>

A spatial model as shown in Fig. 9 where region 2 simulates a cold plume near the exhaust port was created. The plume has volume $V_2 = V_{\mathrm{pl}}$ and temperature T_2. The plume is cylindrical (radius r, length d) with its axis centered on the exhaust port and oriented perpendicular to the tank's axis.

The volume-weighted average temperature for the plume model is given by Eq. (5) with $V_2 = V_{\mathrm{pl}}$. The mode-weighted average temperature from Eq. (6) becomes

$$\langle T \rangle_\varphi = \langle T \rangle_V + \Delta T \left[\frac{V_{\mathrm{pl}}}{V} - \frac{2}{V} \int_{V_{\mathrm{pl}}} |\varphi_l|^2 \, dV \right] . \tag{8}$$

Expressions for V_{p1} and the volume integral are given in Eqs. (B1)-(B2) in Appendix B as functions of l, z_{p}, R, L, r, and h. In Eq. (8), note that difference between $\langle T \rangle_\varphi$ and $\langle T \rangle_V$ is solely due to the plume region because of the axial gradients that exist there. If we set $V_{\mathrm{pl}} = 0$ (*e.g.* by setting $r = 0$), then $\langle T \rangle_\varphi = \langle T \rangle_V$ as it should be because the temperature gradient is then everywhere perpendicular to the cylinder's axis. This result is consistent with our previous findings [6,9].

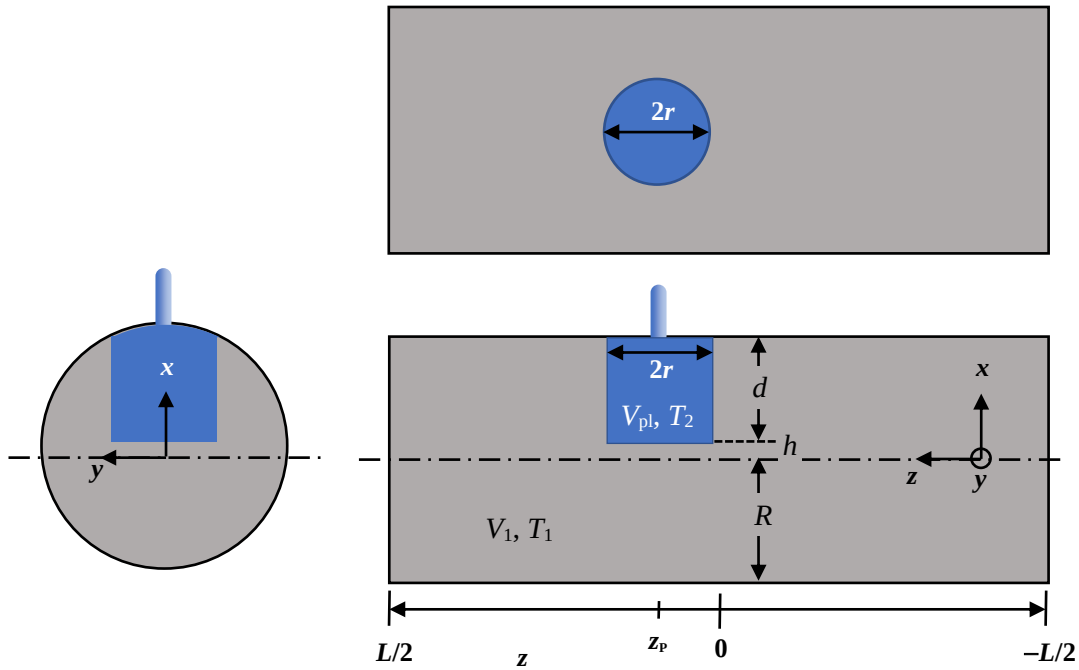

Fig. 9. Geometry of the plume model for the temperature distribution in the tank with the exhaust tube placed at $z = z_P$. The cooler region $T_2 < T_1$ is cylindrical with diameter $2r$ and height d and volume V_{pl}.

The fractional error in $\langle T\rangle_\varphi$ scaled by $T_1 / \Delta T$ is

$$\frac{\langle T\rangle_\varphi - \langle T\rangle_V}{\langle T\rangle_V}\frac{T_1}{\Delta T} = \frac{\left(V_{pl}/V\right) - \left(2/V\right)\int_{V_{pl}} |\varphi_l|^2\, dV}{1 - \left(V_{pl}/V\right)\left(\Delta T/T_1\right)} \ . \tag{9}$$

For $z_p = 0$, *i.e.* the exhaust port is located midway between the ends as it is in the work described here, the integral on the right-hand side of Eq. (9) simplifies to

$$\frac{2}{V}\int_{V_{pl}} |\varphi_l|^2\, dV = \frac{4}{\pi \tilde{L}}\int_0^{\tilde{r}} \cos^2\left(\frac{l\pi\tilde{z}}{\tilde{L}}\right)\left[\sin^{-1}\left(\sqrt{\tilde{r}^2 - \tilde{z}^2}\right) + \sqrt{\tilde{r}^2 - \tilde{z}^2}\left(\sqrt{1 - \tilde{r}^2 + \tilde{z}^2} - 2\tilde{h}\right)\right] d\tilde{z} \ , \tag{10}$$

where the tilde over a variable indicates that the variable has been reduced by R, *e.g.* $\tilde{z} = z/R$. The general case $z_p \neq 0$ is given in Eq. (B2) in Appendix B. Equation (9) is plotted in Fig. 10a as a function of h/R with $2r = R - h$ for $z_P = 0$. For $\Delta T = 5$ K and $T_1 = 295$ K, the maximum error in $\langle T\rangle_\varphi$ for the $l = 2$ mode is about –0.3 %. The effect of locating the exhaust port off center is shown in Fig. 10b, which is a plot of Eq. (9) as a function of z_P / L for $h = 0$ and $2r = R$. The error in $\langle T\rangle_\varphi$ for the plume model for $l = 2$ and 6 is zero for $z_P = L/8$.

Extended plume model

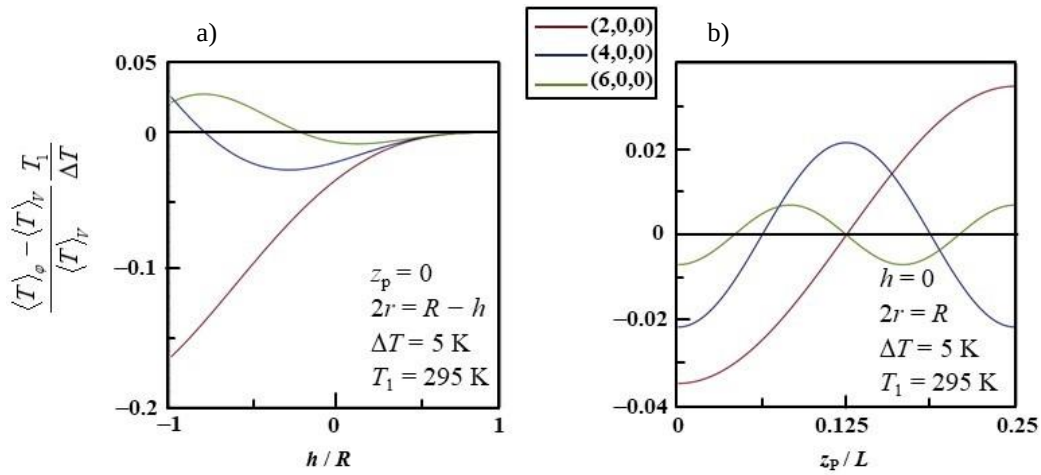

Fig. 10. Plume model. Fractional error in the mode-average temperature scaled by $T_1/\Delta T$ from Eq. (9) for modes l = 2, 4, and 6: a) as a function h/R with $2r = R - h$ and $z_P = 0$, b) as a function of z_P/L with $h = 0$ and $2r = R$.

The temperature distribution in Fig. 11 is an extension of plume model in which cold gas from the plume has collected in the bottom portion of the tank. Region 1 is the top portion of the cylindrical tank with volume V_1 and temperature T_1. Region 2 is at the bottom of the tank, with depth $H = R + h$ and volume V_2', plus the plume volume V_{pl}. The total volume of region 2 is $V_2 = V_2' + V_{pl}$. The plume volume V_{pl} is given by Eq. (B1) in Appendix B. Expressions for the ratios V_2'/V and V_2/V are given in Eqs. (B3) and (B4), respectively. The total volume of tank is the sum $V = \pi R^2 L = V_1 + V_2$.

The volume-weighted average temperature for the extended plume model is given by Eq. (5) with $V_2 = V_2' + V_{pl}$

$$\langle T \rangle_V = T_1 - \left(V_2' + V_{pl}\right)\frac{\Delta T}{V} \ . \tag{11}$$

The mode-weighted average temperature for the extended model is the same as Eq. (8) with $\langle T \rangle_V$ given by Eq. (11). The fractional difference is

$$\frac{\langle T \rangle_\varphi - \langle T \rangle_V}{\langle T \rangle_V}\frac{T_1}{\Delta T} = \frac{\left(V_{pl}/V\right) - \left(2/V\right)\int_{V_{pl}} |\varphi_l|^2 \, dV}{1 - \left(V_2/V\right)\left(\Delta T/T_1\right)} \ . \tag{12}$$

The numerator is the same as the plume model. The only difference between Eq. (12) and Eq. (9) is the volume $V_2 = V_2' + V_{pl}$ in the denominator instead of just V_{pl}. Unless ΔT is very large compared to T_1, the plots in Figs. 10a and 10b are indistinguishable between the plume model and the extended plume model. Most importantly with both models, the error in $\langle T \rangle_\varphi$ for l = 2 and 6 is zero for $z_P = L/8$.

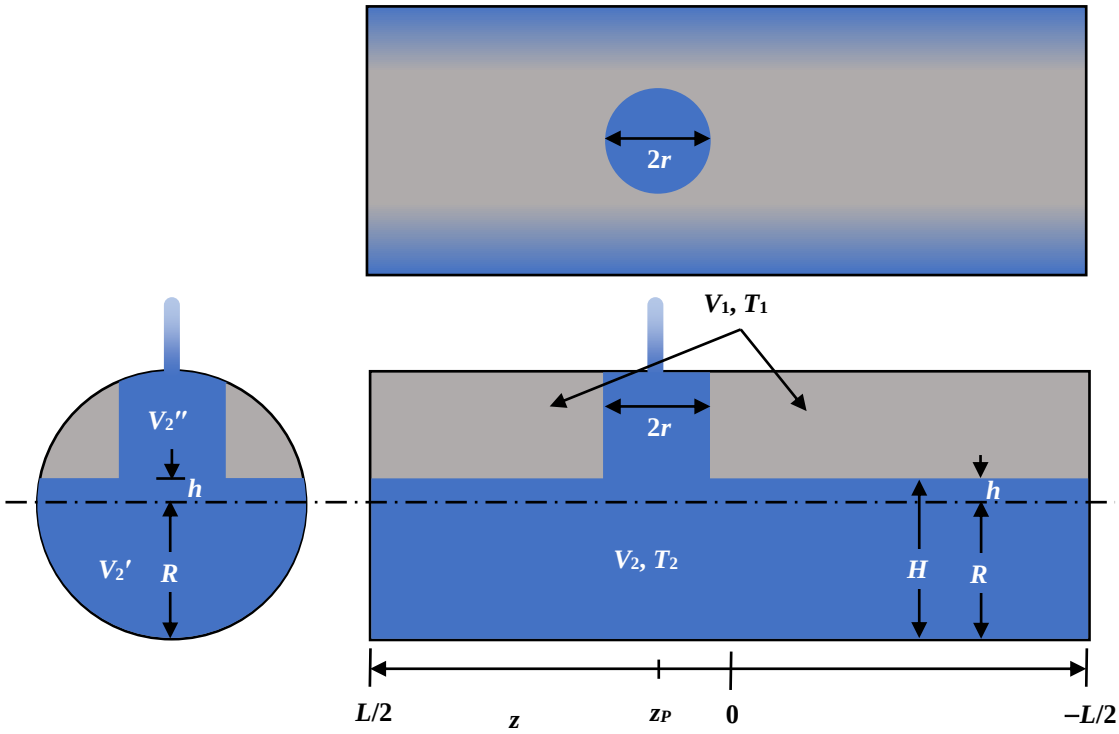

Fig. 11. Extended plume model. Step function temperature distribution in the tank based on the shell thermocouple measurements. We explore the calculated acoustic temperature as a function of the exhaust port location z_P.

The actual temperature distribution in the cylindrical tank is likely a complicated combination of the plume model and the extended model that depends on initial conditions and the duration of flow, which may differ for each flow. We believe this to be the reason for the offset and standard deviation in $\dot{m}_{\mathrm{acst}}$ in Table 1.

For the measurements in this work, the cylindrical tank exhaust port is located at its center where the temperature of the cool, expanding gas in the vicinity is being weighted strongly by the acoustic wave, as implied by Fig. 8. According to our models, if the exhaust port was located a distance $L/8$ from the center, this problem will be minimized for the (2,0,0) and (6,0,0) modes, shown in Fig. 10.

IV. Uncertainty

We follow the guidelines for evaluating and expressing uncertainty provided in NIST TN 1297 [33], the ISO Guide to Uncertainty in Measurement [34], and elsewhere [35]. Equation (3) relates the measurand, $\dot{m}_{\mathrm{acst}}$, to n measured input variables, x_{i}. The combined relative uncertainty of the measured acoustic mass flow is determined using the propagation of uncertainty formula:

$$u^2\left(\dot{m}_{\mathrm{acst}}\right)=\sum_{i=1}^{n} S_{x_i}^2 u^2\left(x_i\right) \quad , \tag{13}$$

where $u^2(\dot{m}_{\mathrm{acst}})$ is the combined standard uncertainty in $\dot{m}_{\mathrm{acst}}$, $S_{x_i} = \left(\partial \dot{m}_{\mathrm{acst}} / \partial x_i\right) x_i / \dot{m}_{\mathrm{acst}}$ is the dimensionless sensitivity coefficient of x_i on $\dot{m}_{\mathrm{acst}}$, and $u(x_i)$ is the standard relative uncertainty in x_i. The combined standard relative uncertainty (u_c) is multiplied by the coverage factor (k = 2) to obtain the combined expanded relative uncertainty (U_e).

Uncertainty evaluations for NIST calibrated CFVs used as flow references have been published elsewhere and will not be covered in detail here [2,4,10,36]. $U_e(\dot{m}_{\mathrm{CFV}})$ is 0.18 % for flows less than 1.7 g/s. For flows between 1.7 g/s and 12.4 g/s, temperature gradients due to the cold gas exiting the tank led to significant temperature sampling errors, uncertainty in the CFV throat temperature, and $U_e(\dot{m}_{\mathrm{CFV}})$ of 0.77 % [36].

$U_e(\dot{m}_{\mathrm{acst}})$ from the cylindrical tank is 0.52 %, which is an order of magnitude larger than we desire. We root-sum-squared this with our CFV flow uncertainty to get $U_e(\dot{m}_{\mathrm{acst}} - \dot{m}_{\mathrm{CFV}})$ that ranges between 0.54 % to 0.93 %. The largest contribution to the uncertainty in $\dot{m}_{\mathrm{acst}}$ is the standard deviation σ in the repeated measurements of each mode. The standard deviation is on the same order as the average offset in $\dot{m}_{\mathrm{acst}} - \dot{m}_{\mathrm{CFV}}$ that can be seen in Fig. 2 and therefore, we combine these into one uncertainty component. The data points in Fig. 2 represent a minimum of three repeated measurements. The standard deviation of all measurements of each mode at each flow was taken and the maximum value over the flows tested was used in our uncertainty budget. This component contributes approximately 79 % to the overall uncertainty and

Table 1. Uncertainty budget for dynamic acoustic mass flow.

Variable x_i	**S_{xi} [-]**	**$u(x_i)$ [%]**	**$S_{xi}^2 \times u(x_i)^2$**	**Contribution [%]**
Static mass	1	0.017	2.9×10^{-4}	0.4
P_{tank} [kPa]	1	0.012	1.3×10^{-4}	0.2
V_{tank} [m³]	1	0.02	3.3×10^{-4}	0.5
Z_{acst}/Z	1	0.0029	8.6×10^{-6}	> 0.1
k_N [/m]	2	0.025	2.6×10^{-3}	3.9
Perturbations Δf	0.4	0.043	3.0×10^{-4}	0.4
Measurement σ	1	0.23	0.052	79.3
Slope error	1	0.10	0.01	15.2
		u_c	0.26 %	
		U_e	0.52 %	

is 0.23 % as shown in Table 1. We see this variance over our tested flow range including our lowest flow of 0.24 g/s, the flow where $U_e(\dot{m}_{CFV})$ is minimal. Therefore, we believe the variance is due to the acoustic flow measurements. The next largest contribution to the overall uncertainty (approximately 15 %) is the standard uncertainty in the slope of $M_{acst}(t)$. We use the formulations found in [35] to calculate the slope. We used the worst-case scenario of 0.1 % of $\dot{m}_{acst}$ in Table 1, however, the values ranged from 0.02 % to 0.1 % over the flow range presented in Fig. 2. Random noise in pressure and frequency measurements is the source of the error in the slope calculation.

Other sources of uncertainty

The ideal resonance frequency f_N is the theoretical frequency of mode N assuming the resonator has a perfect geometric shape with mechanically rigid, thermally insulating walls and neglecting the transport properties of the enclosed gas. The measured resonance frequency f_m is perturbed from f_N by the effects of openings (ports) in the resonator walls, compliance of the walls, and the thermal and viscous boundary layers in the gas [23]. Therefore, to determine the mass of gas from Eq. (3), f_m must be corrected for these perturbations Δf to calculate f_N : $f_N = f_m - \sum_i \Delta f_i$ [9]. If these corrections are not made, errors in M_{acst} could be as large as that shown in Figure 12a.

We determined the agreement between the gravimetrically and acoustically measured mass of both nitrogen gas and argon gas added to the cylindrical tank. We repeated the experiment performed in our previous work [5] to demonstrate the degree of consistency between these two mass determination methods. Uncertainty in the gravimetric measurement is 0.032 %.

Figure 12 shows $(M_{acst} - M_{grav}) / M_{grav}$ determined from the (2,0,0), (4,0,0), and (6,0,0) modes. Figure 12a shows the percent difference when the cylindrical tank is treated like an ideal resonator with no corrections for perturbations to the measured frequency f_m. Figure 12b shows the difference with the corrections made for perturbations due to the thermoviscous boundary layer, the port for the pressure gauge, the gas inlet (filling) port, and the exhaust port. The largest perturbations are from the exhaust port and the shell recoil, which shift f_m by up to 0.2 % and 0.36 %, respectively. For the (6,0,0) mode, these corrections had the same sign and were additive. For the (2,0,0) and (4,0,0) modes, these corrections had opposite signs, however, the exhaust port perturbation was negligible for the (4,0,0) mode. The thermoviscous boundary layer was the second largest correction for this mode, shifting f_m by up to 0.03 %.

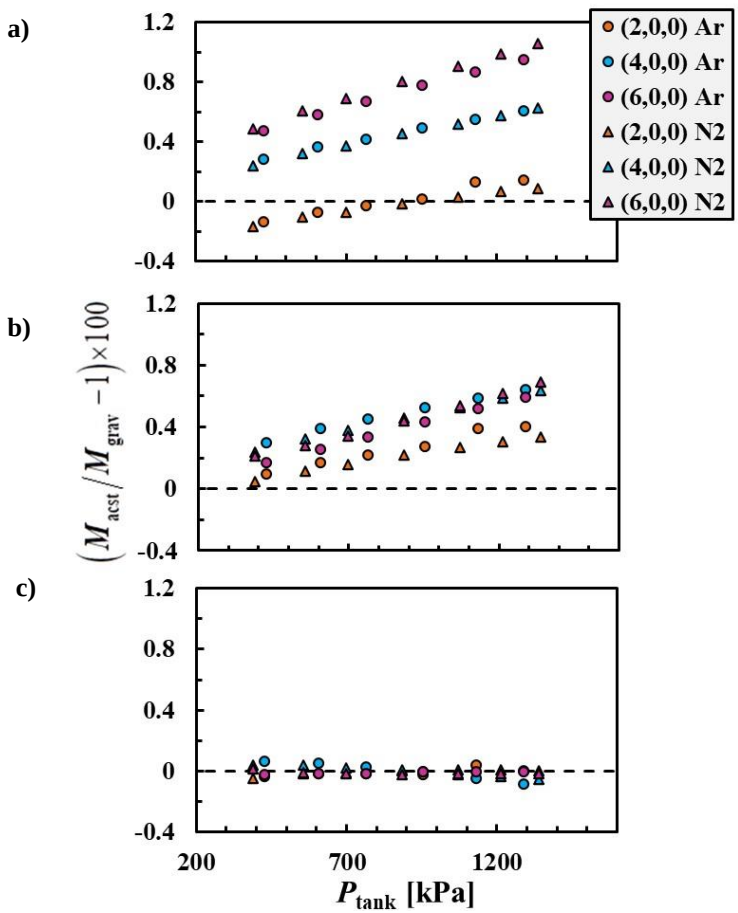

Fig. 12. a) Percent deviations between mass measured acoustically and gravimetrically in the cylindrical tank. b) Deviations with corrections to f_m except for shell recoil. c) Deviations with all corrections including shell recoil.

We fit the deviations in Fig. 12b with a physically motivated function [9] for the shell recoil perturbation:

$$\frac{\Delta f_{l,\mathrm{sh}}}{f_{\mathrm{m}}} = -\left(\rho w^2\right)_{\mathrm{gas}} \frac{C_l + D_l P + E_l P^2}{1-\left(f/f_{\mathrm{sh}}\right)^2} \tag{14}$$

The admittance parameters C_l, D_l, and E_l, and the shell resonance frequency f_{sh} were adjusted to fit all the data, (2 gases, 3 modes, and $P_{\mathrm{tank}} > 200$ kPa) simultaneously. The fitted shell resonance frequency, $f_{\mathrm{sh}} = 836.5$ Hz, was far above the gas mode frequencies measured here. Figure 12c shows the agreement with all corrections added.

For uncertainty in Δf, we took the uncertainty in the gravimetric mass and root-sum-squared it with the deviations from zero in Figure 12c after applying all the calculated perturbations. We assume the difference from zero is due to our ignorance of the corrections and therefore our uncertainty in them.

The uncertainty in f_{m} was determined from the 0.05 Hz noise in the signal and accounted for in the standard

error in the slope calculation. The uncertainty of the pressure sensor based on calibration records is $36 \times 10^{-6}\, P + 54$ Pa. The volume of the cylindrical tank and its uncertainty have been well characterized in a previous publication using microwave resonance frequencies and a gas expansion from a known volume [8]. The acoustic wave number k_N for the cylindrical tank was also determined in a prior publication [9]. The uncertainty in k_N was determined by comparison of the value computed using a finite element model for a cylindrical vessel with ellipsoidal heads. The relative standard uncertainty in k_N for the (2,0,0) and (4,0,0) modes is approximately 0.01 % and 0.025 % for the (6,0,0) mode, which is used in Table 1. The real gas correction $\mathcal{Z}_{\mathrm{acst}}/Z$ is the correction for 1) the acoustic pressure, which is the squared ratio of the speed of sound to its zero-pressure value, and 2) the gas compressibility factor. Using the REFPROP [37] uncertainty values for both w and ρ for nitrogen, we found the uncertainty in $\mathcal{Z}_{\mathrm{acst}}/Z$ is negligible as shown in Table 1.

V. Summary and Conclusions

In our previous work we successfully measured the mass of a pure, stagnant gas in spherical and cylindrical pressure vessels using acoustic resonance techniques. We also investigated measuring the mass of gas dynamically during a flow by tracking an acoustic resonance frequency in real time. In this work, we discuss this tracking method that uses self-oscillation and positive feedback. We discuss our current limitations, the uncertainty in determining the mass flow using this technique, and ways to improve acoustic mass flow measurements.

The dynamic tracking method was successful in both tank geometries; however, the spherical geometry was not as well suited as the cylindrical geometry because the even longitudinal modes of a cylindrical tank have a relatively high amplitude and are more isolated from the other modes. In the cylindrical vessel, we were successful at tracking $f_N(t)$ of three longitudinal modes during flows up to 12.4 g/s. We did not investigate flows larger than this because the cylindrical tank volume and pressure rating are not large enough to flow for sufficient time to determine the slope of M_{acst} versus time with the desired uncertainty.

We speculate that the systematic offset and standard deviation in $\dot{m}_{\mathrm{acst}} - \dot{m}_{\mathrm{CFV}}$ shown in Fig. 2 are due to temperature gradients forming in the axial direction of the cylindrical tank. These temperature gradients are complex and not easily reproduced leading to errors in the acoustic temperature that vary with each flow experiment.

This work was limited, in part, by the instrumentation. The parametric equalizer was not controlled by computer; therefore, the filter and delay parameters had to be manually adjusted during the flow to compensate for the changing frequency. Computer-controlled instrumentation for filter and delay adjustments during flow would allow tracking for large flows that cause the acoustic resonance frequency to move outside of the initial filter pass band. We did not have this problem with the flows tested in the cylindrical tank because the modes were isolated.

From this work, we learned design rules for an acoustic flow standard, e.g., 1) the exhaust port location should be optimized based on the modal nodes and antinodes and expected temperature gradients in order to minimize the difference between $\langle T \rangle_\varphi$ and $\langle T \rangle_V$; locating the exhaust port on the bottom of the tank would reduce plume and buoyancy effects of cold gas otherwise exiting through the top, 2) a thick walled tank without a rigid base and minimal welds diminishes shell recoil effects, and 3) the tank should have high pressure rating and/or *large* volume to provide enough gas for "large" flows without increasing the uncertainty in $\dot{m}_{\mathrm{acst}}$ above the desired value. The tank capacity would be determined by the largest flow target. In addition to these needs for the resonator, we need 1) better acoustic resonance frequency tracking instrumentation and software and 2) a lower uncertainty flow reference to compare with $\dot{m}_{\mathrm{acst}}$. Adding a heat exchanger upstream from the CFV would reduce the uncertainty of the reference flow if it were well instrumented to make corrections for storage effects caused by gas density changes within the heat exchanger [38].

Our uncertainty in $\dot{m}_{\mathrm{acst}}$ is 0.51 % in this work. The standard deviation of the measurements σ contributes more than 79 % to our overall uncertainty in $\dot{m}_{\mathrm{acst}}$. The second largest contributor is the standard error in the slope of M_{acst} versus time. We can reduce the latter if we measure the flow for a sufficiently long time that the noise in the measurement of P/f^2 becomes insignificant. Our goal is to make this standard error in the slope less than 0.01 %. The challenge is σ. If our predictions about the location of the exhaust port are correct and we can reduce σ to less than 0.01 %, then we can reduce our uncertainty in $\dot{m}_{\mathrm{acst}}$ to 0.12 %. The largest contribution would then be from the wave number k_N. However, we can make better measurements to lower the uncertainty in k_N by calibrating the resonator with a known gas at a known temperature [21]. If we can reduce the uncertainty in k_N to within 0.02 %, then our overall expanded uncertainty in the $\dot{m}_{\mathrm{acst}}$ will be 0.08 %. Therefore, 0.08 % is our target uncertainty for the next generation acoustic gas flow standard.

Acknowledgements

The authors would like to thank James B. Mehl for his finite element analysis of the cylindrical tank, Michael R. Moldover for his physical insight and suggestions, and James B. Filla for his expertise and help with LabView programming.

Appendix A. Automatic Gain Control

The general function of the Automatic Gain Control circuit (AGC) is shown in Figure 13a. Its purpose is to amplify input signals with small amplitudes so that self-oscillation of the acoustic mode is sustained; and to attenuate signals with large amplitudes to avoid clipping. Ideally the circuit is designed such that the overall gain of the acoustic resonator is unity without clipping and with a constant phase for a wide range of mode amplitudes.

The present implementation Figure 13 uses a light emitting diode (LED) and a light dependent resistor (LDR) for which the dark resistance (~250 kΩ) decreases with increasing light intensity. The ac signal is rectified, then filtered with a capacitor to smooth out the pulses to yield a dc signal proportional to the amplitude of the input acoustic signal.

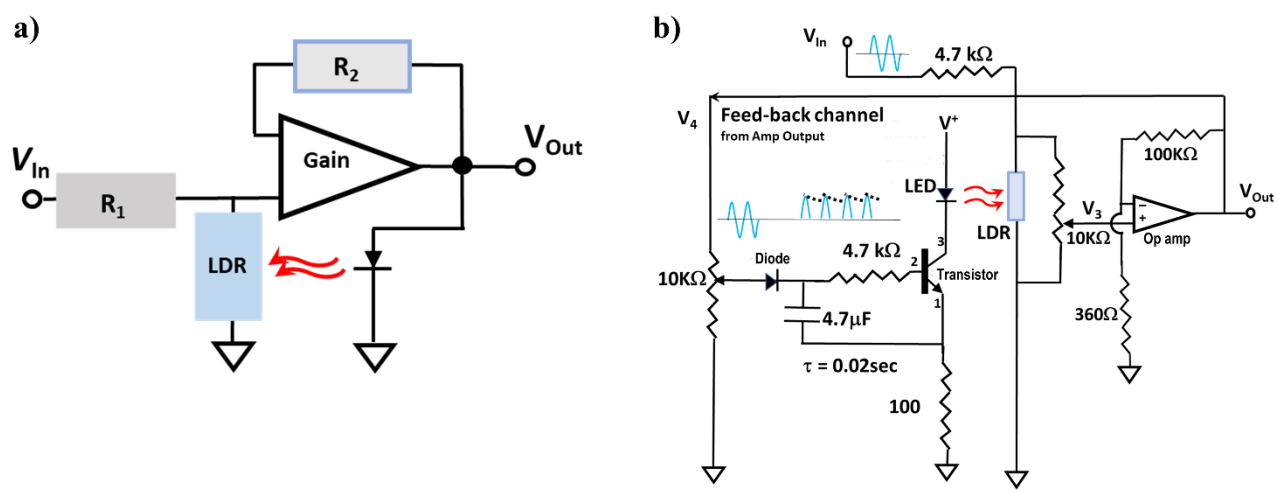

Fig. 13. a) shows the general concept of the automatic gain control (AGC) using an inexpensive light dependent resistor, (LDR) that converts light intensity to a change in resistance. b) shows the specific circuit used in the present work. The circuit is based on Ref. [30]. LED: Kingbright # WP710A10LSECK/J3; Diode: onsemi # 1N914A; Transistor: onsemi # 2N3904; General purpose Op amp # LM741.[2]

Appendix B. Temperature Model Calculations

The temperature distribution for the plume model is shown in Fig. 9. The volume-weighted average temperature is given in Eq. (5) with $V_2 = V_{pl}$, and the mode-weighted average temperature is given in Eq. (8). The volume of the plume is

$$V_{\mathrm{pl}} = \frac{4R^3}{3}\left\{\left[1+\left(\frac{r}{R}\right)^2\right]E\left(\frac{r}{R}\right)-\left[1-\left(\frac{r}{R}\right)^2\right]K\left(\frac{r}{R}\right)\right\}-\pi r^2 h \ . \tag{B1}$$

Converting to dimensionless variables $\tilde{r} \equiv r/R$, $\tilde{L} \equiv L/R$, $\tilde{h} \equiv h/R$, $\tilde{z}_{\mathrm{p}} \equiv z_{\mathrm{p}}/R$, and $\tilde{z}'' \equiv \left(z - z_{\mathrm{p}}\right)/R$, then integrating over *x* and *y*, the volume integral in Eq. (8) becomes

$$\frac{2}{V}\int_{V_{\mathrm{pl}}} |\varphi_l|^2 \, dV = \frac{2}{\pi\tilde{L}}\int_{-\tilde{r}}^{\tilde{r}} \cos^2\left(\frac{l\pi\left(\tilde{z}''+\tilde{z}_{\mathrm{p}}\right)}{\tilde{L}}\right)\left[\sin^{-1}\left(\sqrt{\tilde{r}^2-\tilde{z}''^2}\right)+\sqrt{\tilde{r}^2-\tilde{z}''^2}\left(\sqrt{1-\tilde{r}^2+\tilde{z}''^2}-2\tilde{h}\right)\right]d\tilde{z}'' . \tag{B2}$$

The fractional difference between the volume-weighted and mode-weighted average temperatures is given in Eq. (9).

The extended plume model is shown in Fig. 11. The volume V_2' is given by the expression

$$\frac{V_2'}{V} = 1-\frac{1}{\pi}\cos^{-1}\left(\frac{h}{R}\right)+\frac{h}{\pi R}\sqrt{1-\left(\frac{h}{R}\right)^2} \ , \tag{B3}$$

and the plume volume V_{pl} is given by Eq. (B1). The total volume V_2 for the extended plume model is, therefore,

$$\begin{aligned}\frac{V_2}{V} = \frac{V_2'}{V}+\frac{V_{\mathrm{pl}}}{V} &= 1-\frac{1}{\pi}\cos^{-1}\left(\frac{h}{R}\right)+\frac{h}{\pi R}\sqrt{1-\left(\frac{h}{R}\right)^2}-\frac{r^2 h}{R^2 L} \\ &\quad +\frac{4}{3\pi}\frac{R}{L}\left[\left(1+\left(\frac{r}{R}\right)^2\right)E\left(\frac{r}{R}\right)-\left(1-\left(\frac{r}{R}\right)^2\right)K\left(\frac{r}{R}\right)\right] \\ &\approx 1-\frac{1}{\pi}\cos^{-1}\left(\frac{h}{R}\right)+\frac{h}{\pi R}\sqrt{1-\left(\frac{h}{R}\right)^2}+\frac{R}{L}\left(\frac{r}{R}\right)^2\left[1-\frac{h}{R}-\frac{1}{8}\left(\frac{r}{R}\right)^2\right]+\mathrm{O}\left[\left(\frac{r}{R}\right)^6\right]\end{aligned} \tag{B4}$$

The volume-weighted average temperature $\langle T\rangle_V$ is given by Eq. (11) and the mode-weighted average temperature $\langle T\rangle_\varphi$ is the same as Eq. (8) with $\langle T\rangle_V$ given by Eq. (11). The difference $\langle T\rangle_\varphi - \langle T\rangle_V$ is the same for both models and is dependent on the plume geometry. The fractional difference between the mode-weighted average temperature and the volume average temperature is given in Eq. (12).

References

[1] J. D. Wright, S.-I. Nakao, A. N. Johnson, and M. R. Moldover, "Gas flow standards and their uncertainty," Metrologia, 2022 (in press). https://doi.org/10.1088/1681-7575/ac8c99.

[2] A. N. Johnson, J. D. Wright, "Gas flowmeter calibrations with the 26 m³ *PVTt* standard," NIST Special Publication 250-1046, November 2009. www.https://www.nist.gov/publications/gas-flowmeter-calibrations-26-m3-pvtt-standard

[3] A. N. Johnson, J. D. Wright, M. R. Moldover, and P. I. Espina, "Temperature characterization in the collection tank of the NIST 26 m³ *PVTt* gas flow standard, Metrologia, **40**, 211–216 (2003).

[4] J. D. Wright, A. N. Johnson, M. R. Moldover, and G. M. Kline, "Gas flowmeter calibrations with the 34 L and 677 L *PVTt* standards," NIST Special Publication 250-63, November 2010. www.nist.gov/publications/gas-flowmeter-calibrations-34-l-and-677-l-pvtt-standards

[5] J. G. Pope, K. A. Gillis, M. R. Moldover, J. B. Mehl, and E. Harman, "Progress towards a gas-flow standard using microwave and acoustic resonances," Flow Meas. Instrum. **69**, 101592 (2019). https://doi.org/10.1016/j.flowmeasinst.2019.101592

[6] J. G. Pope, K. A. Gillis, M. R. Moldover, J. B. Mehl, and E. Harmon, "Characterizing gas-collection volumes with acoustic and microwave resonances," 10th International Symposium on Fluid Flow Measurements, ISFFM, Queretaro, MX, March 21-23, 2018. www.nist.gov/publications/characterizing-gas-collection-volumes-acoustic-and-microwave-resonances

[7] K. A. Gillis, M. R. Moldover, and J. B. Mehl, "Detecting leaks in gas-filled pressure vessels using acoustic resonances," Rev. Sci. Instrum. **87**, 054901 (2016).

[8] M. R. Moldover, J. W. Schmidt, K. A. Gillis, J. B. Mehl and J. D. Wright, "Microwave determination of the volume of a pressure vessel," Meas. Sci. Technol. **26**, 015304 (2015).

[9] K. A. Gillis, J. B. Mehl, J. W. Schmidt, and M. R. Moldover, "'Weighing' a gas with microwave and acoustic resonances," Metrologia **52**, 337–352 (2015).

[10] J. D. Wright, A. N. Johnson, M. R. Moldover, and G. M. Kline, "Errors in rate-of-rise gas flow measurements from flow work," 10th International Symposium on Fluid Flow Measurement, ISFFM, Queretaro, MX, March 21-23, 2018. https://tsapps.nist.gov/publication/get_pdf.cfm?pub_id=925028

[11] A. N. Johnson, E. Harmon, and J. T. Boyd, "Blow-down calibration of a large ultrasonic flow meter," Flow Meas. Instrum, **77**, 101848 (2021). https://doi.org/10.1016/j.flowmeasinst.2020.101848

[12] J. Helffrich and S. Fulop, "The phase-locked loop as a tool for signal analysis," Proc. Mtgs. Acoust. **30**, 055012 (2017). https://doi.org/10.1121/2.0000771

[13] Y. Kuang, Y. Jin, S. Cochran, and Z. Huang, "Resonance tracking and vibration stablilization for high power ultrasonic transducers," Ultrasonics **54**, 187–194 (2014). http://dx.doi.org/10.1016/j.ultras.2013.07.001

[14] N. Chen, S. Fan, and D. Zheng, "A phase difference measurement method based on strong tracking filter for Coriolis mass flowmeter," Rev. Sci. Instrum. **90**, 075003 (2019); doi: 10.1063/1.5086714

[15] F. Leach, S. Karout, F. Zhou, M. Tombs, M. Davy, and M. Henry, "Fast Coriolis mass flow metering for monitoring diesel fuel injection," Flow Meas. Instrum. **58,** 1–5 (2017). http://dx.doi.org/10.1016/j.flowmeasinst.2017.09.009

[16] J. Lu, "Lock-in frequency measurement with high precision and efficiency," Rev. Sci. Instrum. **91**, 075106 (2020); doi: 10.1063/5.0002377

[17] N. D. Smith, "A technique for continuous measurement of the quality factor of mechanical oscillators," Rev. Sci. Instrum. **86**, 053907 (2015). http://dx.doi.org/10.1063/1.4920922

[18] K. A. Gillis, "Fast tracking of acoustic resonance frequencies in large collection volumes to measure flow," 176th Meeting of the Acoust. Soc. Am., Victoria, BC, Canada, November 9, 2018.

[19] T. Borowski, A. Burd, M. Suchenek, and T. Starecki, "Improved photoacoustic generator," Int. J. Thermophys. **35**, 2302–2307 (2014). DOI 10.1007/s10765-014-1751-9

[20] M. R. Moldover, J. P. M. Trusler, T. J. Edwards, J. B. Mehl, and R. S. Davis, "Measurement of the universal gas constant *R* using a spherical acoustic resonator," J. Res. Natl. Bur. Stand. **93**, 85–144 (1988).

[21] K. A. Gillis, "Thermodynamic properties of two gaseous halogenated ethers from speed-of-sound measurements," Int J. Thermophys. **15**, 821–847 (1994).

[22] M. R. Moldover, R. M. Gavioso, J. B. Mehl, L. Pitre, M. de Podesta, and J. T. Zhang, "Acoustic Gas Thermometry," Metrologia **51**, R1–R19 (2014).

[23] M. R. Moldover, J. B. Mehl, and M. Greenspan, "Gas-filled spherical resonators: Theory and experiment," J. Acoust. Soc. Am. **79**, 253-272 (1986).

[24] J. P. M. Trusler, *Physical Acoustics and Metrology of Fluids*, (Adam Hilger, Bristol, England, 1991).

[25] B. Gyüre, B. G. Márkus, B. Bernáth, F. Murányi, and F. Simon, "A time domain based method for the accurate measurement of Q-factor and resonance frequency of microwave resonators," Rev. Sci. Instrum. **86**, 094702 (2015). http://dx.doi.org/10.1063/1.4929865

[26] B. Gyüre-Garami, O. Sági, B. G. Márkus, and F. Simon, "A highly accurate measurement of resonator Q-factor and resonance frequency," Rev. Sci. Instrum. **89**, 113903 (2018).

[27] J. Courtois, and J. Hodges, "Coupled-cavity ringdown spectroscopy technique," Optics Letters, **37**, 3354-3356 (2012). https://tsapps.nist.gov/publication/get_pdf.cfm?pub_id=911352

[28] R. Chen, Z. Peng, M. Wang, A. Yan, S. Li, S. Huang, M.-J. Li, and K.P. Chen, "Spatially resolved fibre cavity ring down spectroscopy," Sci. Reports **10**, 20167 (2020). https://doi.org/10.1038/s41598-020-76721-y

[29] M. Suchenek and T. Borowski, "Measuring Sound Speed in Gas Mixtures Using a Photoacoustic Generator," Int. J. Thermophys. **39**, 11 (2018).

[30] The automatic gain control circuit used in this work was derived from one that uses an LED and an LDR (Light Dependent Resistor) described by Peter Parker (https://www.youtube.com/watch?v=C4g7QRmFnr8).

[31] A. N. Johnson, E. Harman, J. Boyd, "Blow-down calibration of a large 8 path ultrasonic flow meter under quasi-steady flow conditions," The 16th International Flow Measurement Conference, FLOMEKO, Paris, France; August 23-26, 2013.

[32] P. M. Morse and K. U. Ingard, *Theoretical Acoustics* (Princeton University Press, Princeton NJ, 1986). Ch. 11.

[33] B. N. Taylor and C. E. Kuyatt, "Guidelines for the evaluating and expressing the uncertainty of NIST measurement results," NIST TN-1297 (1994).

[34] Guide to the expression of uncertainty in measurement. International Organization for Standardization. 1993; Geneva, Switzerland.

[35] H. W. Coleman and W. G. Steele, *Experimentation and Uncertainty Analysis for Engineers*, 3rd ed. (John Wiley and Sons Inc., New York, 2009).

[36] J. D. Wright, "Performance of Critical Flow Venturis under Transient Conditions", Meas. Sci. Technol., **21** (2010).

[37] E. W. Lemmon, M. O. McLinden, and M. L. Huber, "REFPROP: Reference Fluid Thermodynamic and Transport Properties," NIST Standard Reference Database 23, Version 9.1, Natl. Inst. Stand. and Tech., Boulder, CO, (2010). www.nist.gov/srd/nist23.cfm

[38] J. G. Pope and J. D. Wright, "Performance of Coriolis Meters in Transient Gas Flows", Flow Meas. Instrum., **37**, 42–53 (2014).